Size-Dependent Melting Behavior of Pb-17.5 At. Pct Sb-Free Biphasic Alloy Nanoparticles

M. MANOLATA DEVI, KHUSHUBO TIWARI, and KRISHANU BISWAS

The present investigation reports the size-dependent melting behavior of bi-phasic Pb-17.5 at. pct Sb-free alloy nanoparticles, consisting of face-centered cubic (Pb) and rhombohedral (Sb) phases. These free nanoparticles (devoid of matrix) were synthesized *via* the solvothermal route, and subsequently different sizes were obtained by controlled heat treatment at 373 K under protective Ar atmosphere for the various durations. DSC and *in situ* TEM studies were used to probe the melting behavior. The experimental results reveal classical behavior, indicating the normalized eutectic temperature was inversely proportional to the nanoparticle radius. The *in situ* TEM investigation shows that melting initiates at the triple point among (Pb)/(Sb) and an outer surface and subsequently the melt front propagates into (Pb) phase first and then into (Sb) phase. Detailed thermodynamic modeling of the Pb-Sb system with size was carried out to decipher the size-dependent melting behavior of the biphasic nanoparticles. The experimental finding was corroborated with a theoretically predicted phase diagram as a function of size showing a reasonable match.

https://doi.org/10.1007/s11661-019-05275-0

I. INTRODUCTION

IN the field of nanoscience and nanotechnology, nanoalloys have been one of the most focused areas of research worldwide for the last 2 decades, owing to their extraordinary physical, chemical, mechanical and electronic properties compared with their bulk counterparts as well as constituent metals.[1] They have been extensively explored for a variety of applications including electronics, catalysis, sensors, optical markers, structural components, magnetic data storage and biomedicine.[2–4] The novel and futuristic applications of the nanoalloys necessitate intelligent manipulation of their composition, shape and size during synthesis and subsequent processes to obtain the best combination of properties.[5–8] Therefore, understanding the fundamental properties of the nanoalloys is of tremendous importance to extend their application as a source of new materials for nanotechnology. However, it has been widely realized that the thermal stability of nanoalloys is the most critical issue in the applications, affected by size and alloying at the nanoscale. The critical applications in catalysis, electronic and magnetic data storage require their stability against temperature fluctuation during use. Thus, it is important to understand the fundamental aspects controlling the thermal stability of nanoalloys, which can be investigated by studying their melting behavior. The melting behavior of nanoalloys can provide in-depth understanding of the thermal stability, alloying at the nanoscale and ability of these materials to sustain a nanocrystalline nature at high temperature.

It is to be noted that nanoalloys can be either single or multiphase. In the last 2 decades, extensive research has been carried out on the melting behavior of single-phase nanoalloys.[9–11] Although some studies have reported on multiphase nanoalloys, most of these studies are focused on nanoparticles embedded in a matrix. These studies have categorically shown that the interface between the nanoparticle and matrix plays a significant role in the thermal stability and melting behavior of embedded nanoalloys.[12–16] Therefore, the effect of the matrix on the phase transformation behavior of the embedded system cannot be decoupled, which in turn limits the possibility to investigate the intrinsic melting behavior of the nanoalloys.[17] The aforementioned applications require understanding of the intrinsic thermal stability of the nanoalloys. Hence, to probe the size effect on the intrinsic behavior, the alloy nanoparticles should have free surfaces, *i.e.*, the surfaces need not be confined by matrix. It is important to note here that some studies on free single-phase nanoalloys have been reported in the literature.[9,10,18] However, limited investigations have been

M. MANOLATA DEVI, KHUSHUBO TIWARI, and KRISHANU BISWAS are with the Department of Material Science and Engineering, Indian Institute of Technology, Kanpur 208016, India. Contact e-mail: kbiswas@iitk.ac.in

Manuscript submitted October 8, 2018.

M. Manolata Devi and Khushubo Tiwari contributed equally to the work.

Article published online May 29, 2019

carried out on free multiphase nanoalloys. Since the multiphase nanoalloys are distinctly different and relatively complex compared to single-phase nanoalloys, the investigation on the melting behavior of the multiphase nanoalloys is expected to provide in-depth understanding of the thermal stability and alloying behavior at the nanoscale.

The thermal stability of the free multiphase nanoalloys also requires detailed thermodynamic analyses of the nano-sized systems. As the size of the nanoparticles decreases, the surface as well as interfacial energy makes a significant contribution to the total Gibbs free energy of the nanoalloys. This will affect the thermal stability of the nanoalloys. In general, the contribution of strain energy in the total free energy needs to be used for embedded nanoparticles.[19–21] However, the strain energy for free nanoparticles can be ignored as they are not surrounded by a matrix. Hence, it is important to expand the thermodynamic description of the phases in the nanoalloys for understanding the melting behavior. Although several attempts have been made to calculate the size-dependent nanoalloy phase diagram,[11,22–27] very limited experimental studies have been devoted to this because of the difficulty of investigating phase stability as a function of temperature, size and composition. To date, no comparison with the predicted phase diagram has been reported for multiphase nanoalloys.

In the present investigation, an attempt has been made to understand the size-dependent melting behavior of the biphasic Pb-Sb nanoalloys by combining an experimental investigation with theoretical calculations. Pb-Sb was chosen as a model system.[28] The equilibrium phase diagram of the binary Pb-Sb alloy system exhibits a eutectic reaction at 524.7 K for Pb-17.5 at. pct Sb [L $\rightarrow$ (Pb) + (Sb)] with two terminal solid solutions: face centered cubic (Pb) and rhombohedral (Sb). The maximum solubility of Sb in Pb is 5.8 at. pct and Pb in Sb is 1.9 at. pct at 524.7 K.[28] In the present study, we successfully synthesized free multiphase Pb-Sb alloy nanoparticles by using a solvothermal route. The as-synthesized samples were subsequently heat treated at 373 K for varying durations (1, 2, 4, 8, 12, 16 and 30 hours) under Ar atmosphere to prepare ranges of particle size. Furthermore, differential scanning calorimetry (DSC) and *in situ* TEM were extensively utilized to determine the size-dependent melting behavior of nanoparticles. Furthermore, the equilibrium phase diagram of the Pb-Sb alloy system was investigated at the nanoscale using detailed thermodynamic calculations. The effect of nanoparticle size on melting temperature was investigated. Based on the experimental results and calculated data, efforts were made to develop a quantitative relationship between the melting temperatures of the alloy nanoparticles as a function of particle size.

II. METHODS AND MATERIALS

A. *Sample Preparation*

Free alloy nanoparticles having a composition of Pb-17.5 at. pct Sb were prepared *via* the solvothermal route using lead acetate (Pb $(C_2H_3O_2)_2{\cdot}3H_2O$) and antimony chloride ($SbCl_3$) as a precursor for Pb and Sb, respectively. Sodium borohydride ($NaBH_4$) and N, N-dimethyl formamide (DMF) were utilized in the reaction as reducing agent and solvent, respectively. In a typical reaction, 1.65 mmol of Pb $(C_2H_3O_2)_2.\ 3H_2O$ and 0.35 mmol of $SbCl_3$ were dissolved in 80 ml of DMF followed by the transfer of the mixture to a 100-ml container (Teflon-lined). Following this, 0.23 g of $NaBH_4$ was slowly added to the solution. Subsequently, this filled reactant Teflon container was sealed in an autoclave and kept inside an oven at 413 K for 8 hours. The final product was collected after washing several times using a mixture of high-purity isopropyl alcohol and water. The as-synthesized sample was further heat-treated at 373 K for varying times (1, 2, 4, 8, 12, 16 and 30 hours) under Ar atmosphere to obtain different ranges of particle size. Notably, bulk Pb-17.5 at. pct Sb alloy was prepared in a vacuum induction furnace.

B. *Characterization*

For assessing the finer microstructural information, electron microscopic investigations were extensively carried out in Tecnai G^2 UT 20 and TITAN (aberration-corrected TEM, The Netherlands) and FEI microscope operated at 200 and 300 kV, respectively. The composition and nature of each nanoparticle were extensively analyzed using super EDS (energy dispersive spectroscopy) and HAADF (high-angle annular dark field) detectors attached to TITAN. The melting behavior of alloy nanoparticles was probed using a differential scanning calorimeter (DSC1, Mettler Toledo), employing the heating and cooling rate of 20 K/min with an argon gas flow rate of 100 mL/min in the temperature range of 473-973 K. To observe the melting of the individual alloy nanoparticles, *in situ* transmission electron microscopic studies were performed using a GATAN (Gatan Inc.) single-tilt heating holder on a Titan (300KV) microscope. During *in situ* TEM studies, a video sequence of the heating cycle was recorded and analyzed to obtain the melting behavior of the nanoparticles. The temperatures measured during the *in situ* TEM studies were the output of the pre-calibrated heating stage thermocouple. The calibration of the thermocouple showed the accuracy of the temperature measurement $\pm$ 2 K. However, DSC provides better accuracy of the melting temperature.

III. RESULTS

A. *Size, Morphology and Compositional Analyses*

Extensive microstructural investigations were carried out to decipher the size, shape, nature and distribution of alloy nanoparticles using TEM, HAADF and EDS. Figures 1(a) through (d) shows the low magnification bright-field TEM micrographs obtained from the as-synthesized (0 hours) sample as well as the heat-treated samples at 373 K for 8, 16 and 30 hours,

respectively. Most of the nanoparticles were observed to be uniform in size. Most exhibited two distinct contrasts, indicating the two-phase alloy nanoparticle, along with some showing single-contrast nanoparticles. The details concerning the average particle size of each sample are listed in Table I. The average particle size was observed to increase as a function of the heat treatment time at 373 K.

Furthermore, we measured the composition of the individual phases in the biphasic and single-phase particles. The average composition of each phase is reported in Table II. For determination of the exact composition at the interface, the interface needs to be oriented edge on. For free nanoparticles, it is extremely difficult to orient the interface edge on as the nanoparticles move during tilting inside a TEM column. To further ascertain the biphasic nature of alloy nanoparticles, a high-resolution TEM (HRTEM) image of a representative nanoparticle, having two-phase contrasts, was captured and is shown in Figure 2(b). Two distinct lattice fringes were observed. The estimated interplanar spacing was 0.285 nm and 0.310 nm. These can be indexed corresponding to (111) and (101) of Pb and Sb, respectively, implying each nanoparticle is biphasic. The orientation relationship between (Pb) and (Sb) was found to be $(111)_{(Pb)} \parallel (10\bar{1}2)_{(Sb)}$ and $[10\bar{1}]_{(Pb)} \parallel [\bar{1}2\bar{1}0]_{(Sb)}$. Figure 2a shows the corresponding low-magnification TEM image in which the single- and

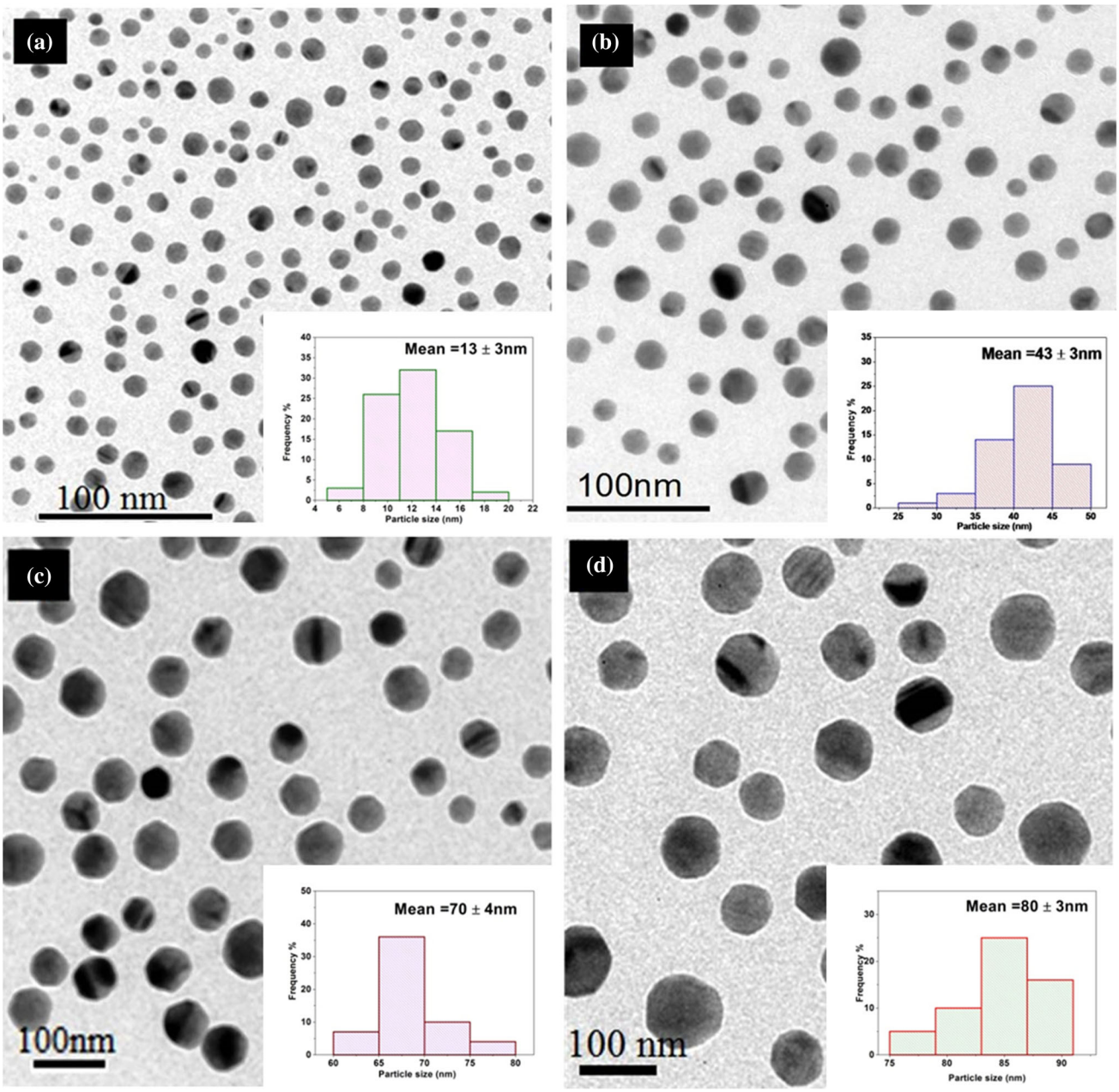

Fig. 1—Bright-field TEM image of Pb-17.5 at. pct Sb after heating at 100 °C under Ar atmosphere for (*a*) 0 h (as-synthesized), (*b*) 8 h, (*c*) 16 h and (*d*) 30 h. Lower inset of each figure shows the particle size distribution histogram.

Table I. Comparison of DSC Data of All Alloy Nanoparticles of Pb-17.5 At. Pct Sb and Counter Bulk Data Along with the Corresponding Particle Size

Sample Condition of Pb-17.5 At. Pct Sb	Heating Cycle (K)			Particle Size (nm)
	Onset Temp.	Peak Temp.	End Set Temp.	
373 K @ 0 h	483.86	501.18	516.94	13 ± 3
373 K @ 1 h	494.94	509.44	523.96	18 ± 2
373 K @ 2 h	496.52	511.46	526.74	23 ± 2
373 K @ 4 h	503.88	515.46	529.74	30 ± 2
373 K @ 8 h	509.55	517.6	536.59	43 ± 3
373 K @ 12 h	513.69	522.36	536.4	55 ± 4
373 K @ 16 h	515.05	521.89	536.5	70 ± 4
373 K @ 30 h	515.57	522.43	537.42	80 ± 3
As cast	525.5	531.5	553.6	bulk

Table II. Composition of Individual Phases Measured Using EDS Attached to TEM

Nanoparticle, Single/Biphasic	Composition (Pb) in Atomic Percent	Composition (Sb) in Atomic Percent
Single	Pb = 98.74 Sb = 1.26	(Sb) was not obtained in the synthesis
Biphasic	Pb = 79.44 Sb = 20.56	Pb = 20.97 Sb = 79.03

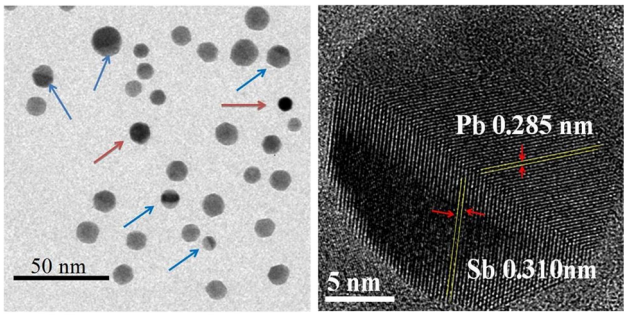

Fig. 2—(*a*) Bright-field TEM micrograph of Pb-Sb alloy having single-phase nanoparticles (red arrow) of Pb-rich nanoparticles along with two-phase alloy nanoparticles (blue arrows). (*b*) HRTEM image of two-phase alloy nanoparticles and (*c*) schematic illustration of an individual biphasic free nanoparticle with cuboctahedral shape (Color figure online).

double-contrast alloy nanoparticles are marked by red and blue arrows, respectively, for more clarity. In fact, the detailed microstructural investigation clearly indicates that biphasic nanoparticles consist of two types of morphologies: cap on body and lamellar. The formation of these two morphologies was dependent on the available volume fraction of the starting precursors (Pb and Sb atoms) during the formation of alloy nanoparticles.[29] However, the population of single-phase alloy nanoparticles was low. The formation of two-phase alloy nanoparticles of Pb-Sb was further confirmed by detailed analysis using HAADF and EDS. Two distinct contrasts in the HAADF image (Figure 3(a)) and an indication of the predominant presence of Pb and Sb in the EDS elemental mapping (Figure 3(b)) and the EDS spectrum (Figure 3(c)) further confirmed the formation of two-phase Pb-Sb alloy nanoparticles. The details on the synthesis and structure of alloy nanoparticles are reported elsewhere.[29]

B. *Melting Behavior*

1. *Differential scanning calorimetric (DSC) study*

To investigate the size-dependent melting temperature of bi-phasic alloy nanoparticles, thermal characterization of all the samples was carried out using DSC. Figures 4(a) and (b) shows the DSC thermograms collected from the as-synthesized sample and samples after heat treatment at 373 K for 4, 8, 12, 16 and 30 hours, respectively. The heating cycle of as-synthesized powder (373 K at 0 h) in Figure 4a shows two endothermic peaks with an onset melting temperature of 483.86 ± 2 K and 580 K, respectively. The equilibrium melting temperatures of pure Pb and Sb (shown by the blue dotted line in Figure 4(a) and eutectic Pb-Sb alloy) are 600.5 K, 903.63 K and 525.5 K, respectively.[28] Therefore, the sharp and symmetrical melting temperature at 483.86 ± 2 K can be attributed to the eutectic temperature of the Pb-Sb alloy. A depression of ~ 41 K compared with the corresponding bulk alloy (525.5 K) can be clearly observed. The second small peak with an onset temperature at 580 K corresponds to Pb-rich solid solution, (Pb) phase, which was observed in the TEM image (Figure 2(a) with red arrow). Similarly, the DSC thermograms of the heat-treated samples were also obtained and are shown in Figure 4(b). Detailed DSC results of all the nanoalloys along with the bulk sample are listed in Table I. One can observe that the melting temperature of eutectic nanoparticles increases as the time of heat treatment

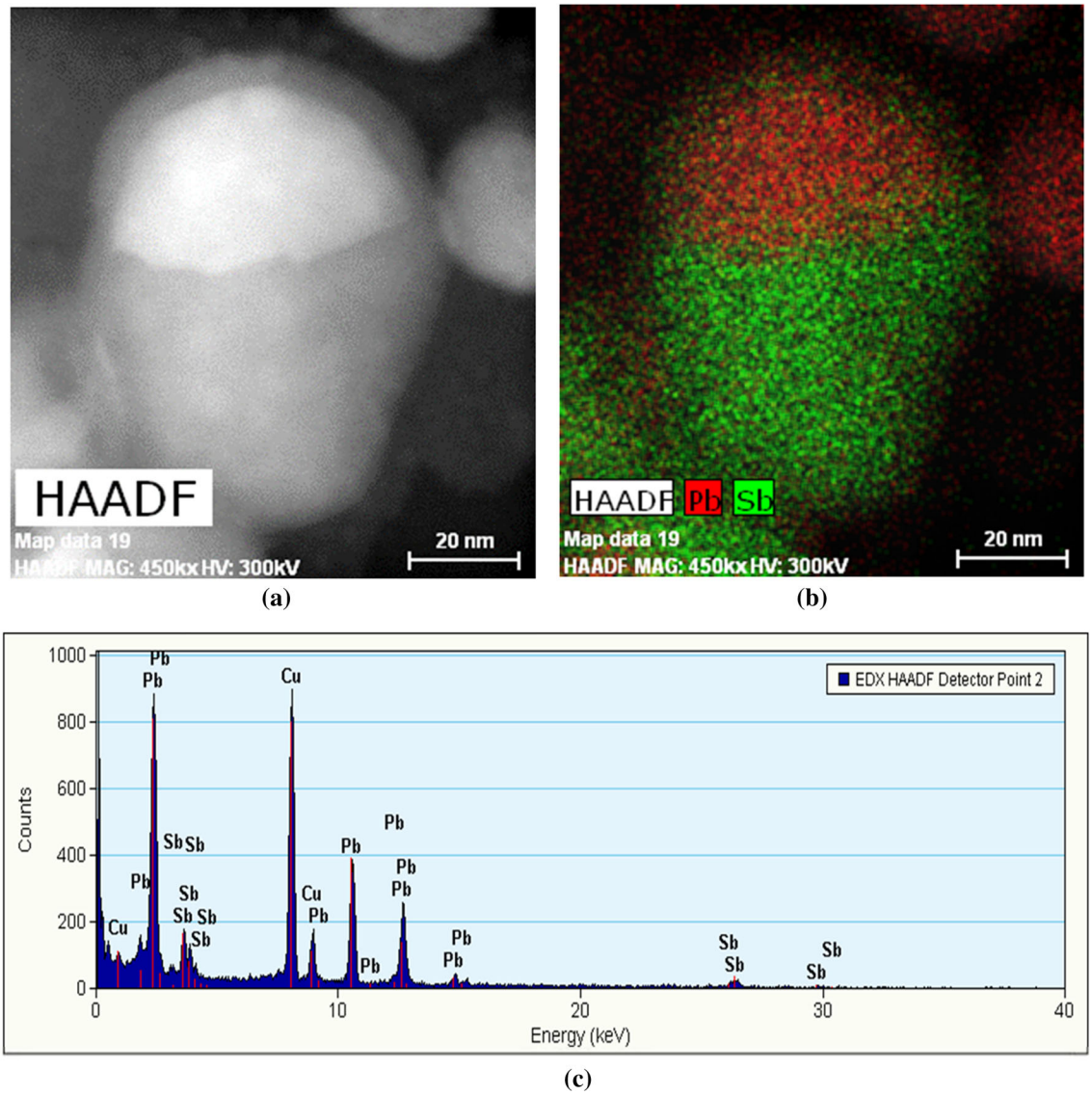

Fig. 3—(*a*) HAADF image, (*b*) EDS elemental maps (corresponding to different elements, Pb and Sb) of alloy nanoparticle revealing alloy phases and (*c*) EDS spectrum from a nanoparticle. Cu peaks are due to the 400-mesh Cu grid used to mount the sample.

increases (or the particle size increases). However, a depression in the melting temperature is observed in each case compared with the bulk alloy. The depression in the melting temperature can be understood by considering the high surface energy to the total energy, because it is likely that melting starts at the surface of the nanoparticles. As the particle size is reduced to the nanoscale, a large fraction of atoms will be occupying the surface, and these surface atoms tend to be unsaturated, resulting in large energy associated with this surface.

2. *In situ heating study*

To observe the melting of such biphasic alloy nanoparticles, *in situ* electron microscopy studies were performed. Notably, the melting experiment was performed by recording a series of bright-field micrographs while heating the sample at a rate of 5 K/min. A Chromel-Alumel thermocouple was attached to the heating specimen stage to record the temperature and is calibrated in such a way that the temperature should not vary by > 2 K. The nanoparticles were in contact with the amorphous carbon thin film on a copper grid while performing the *in situ* TEM investigation. Notably, Pb and Sb exhibit no solubility with carbon. Therefore, it can safely be assumed that each nanoparticle is present independently on the carbon thin film as it does not allow any diffusion through the film while performing the *in situ* experiment. Hence, it was anticipated that it would not affect the thermal equilibrium of the nanoparticles. Figures 5(a) through (n) shows the melting sequence of the ~ 40-nm biphasic nanoparticle. Initially, as the particle was heated up to 507 K, no substantial change in the shape of the nanoparticle was observed. The relative area fractions and facets of both the phases undergo changes during

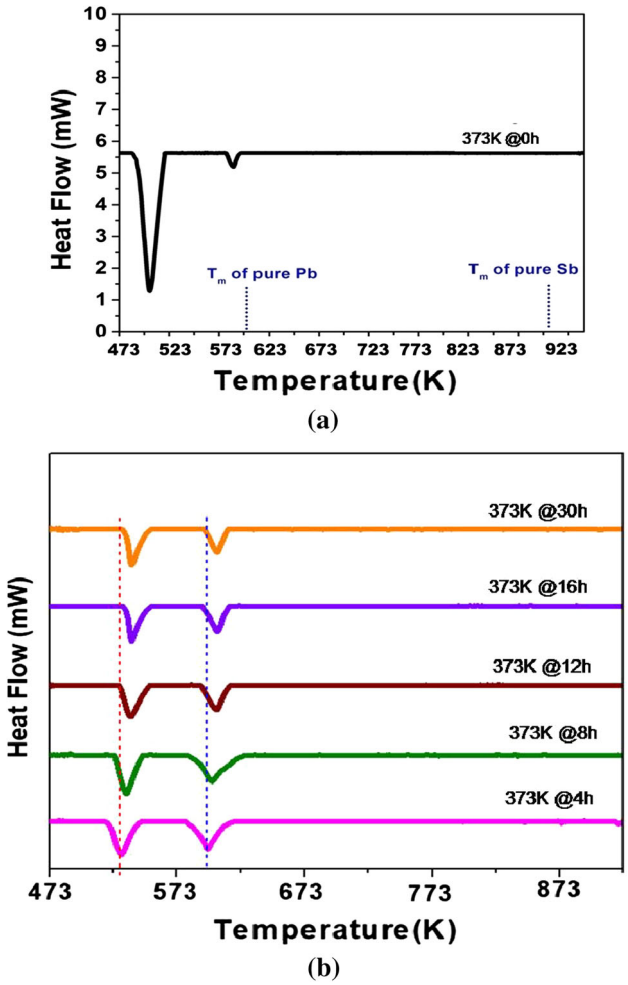

Fig. 4—DSC thermograms of (*a*) as-synthesized Pb-17.5 at. pct Sb alloy nanoparticles and (*b*) samples heat treated at 100 °C for different times.

heating up to 507 K. As soon as the temperature reaches 512 K, a sudden change in the shape at the triple point [interface between (Pb)/(Sb) and the outer surface] appeared, indicating the initiation of melting. The onset melting temperature of ~ 40 nm biphasic particles of Pb-Sb (512 K) is 13.5 K lower than the equilibrium eutectic temperature (525.5 K), which is substantially lower than the DSC data (see Table I). This is primarily due to the difference in sensitivity of the DSC and Chromel-Alumel thermocouple attached to the heating stage used to carry out the *in situ* TEM study. As the temperature was increased, the melt front spread along the surface boundary of the (Pb) phase of the nanoparticle rather than spreading toward the interface between (Pb) and (Sb). As the temperature was raised further, the (Pb) phase was completely melted at 523 K, and subsequently the melt front spread towards (Sb) and the whole particle abruptly became molten at 548 K. For more clarity, the stages of the phase transformation (melting phenomena) are schematically demonstrated in Figure 6(a) through (j). The video of the heating sequence is provided in Supplementary Information (Supplementary Video S1).

IV. DISCUSSION

A. *Thermodynamic Model*

The experimental results clearly reveal that bi-phasic (Pb)-(Sb) free alloy nanoparticles undergo classical melting, *i.e.*, melt nucleates at the triple point ((Pb)/(Sb)/surface). Subsequently, the melt front rapidly propagates into one of the phases (Pb). This is followed by propagation of the melt front into (Sb) and the whole particle melt at 548 K. The DSC data indicate a substantial depression (41 K) of melting temperature, and the melting temperature is observed to be inversely proportional to the size of the nanoparticles. These observations need explanation. In the following section, we attempt to explain the results using a thermodynamic approach by estimating the size-dependent phase diagram of the Pb-Sb system.[30]

The phase diagram has been used for decades as a conventional tool to determine the thermal stability of the phases.[31] Obviously, the phase stabilities of a nanoscaled alloy system are different from the micron-scale system because of the large surface area-to-volume ratio offered by nanosize particles. A few attempts were previously made to predict the phase equilibria of a homogeneous alloy system, Au-Si,[23] Au-Pt,[27] Bi-Sn,[26,32] In-Sn[33,34] and Pb-Sn[14,35,36] embedded in a matrix as a function of nanoparticle size. However, the phase stabilities of the multi-phase system at the nanoscale are more complex as it possesses an extra internal interphase interface with significant capillary energy, which is composition and temperature dependent.[30] As the particle size reduces, the excess free energy increases rapidly and consequently capillary effects affect the thermodynamic equilibrium more significantly.

To predict the size-dependent phase diagram in the present investigation, the method formulated by Weissmuller *et al.*[37] was adopted. However, the theoretical approach by Weissmuller *et al.*[37] cannot be directly applied to a real system because of consideration of the following assumptions: (1) the binary system considered, consisting of the A and B components with equal melting temperature; (2) the composition lying at 50 at. pct B; (3) no solid solubility; (4) the alloy nanoparticles are assumed to be spherical; (5) all the interface energies and molar volumes of all the phases are set as equal. However, in the present study, Pb-Sb is a binary system having a eutectic composition of Pb-17.5 at. pct Sb. Pb and Sb have different melting temperatures, and the maximum solubility of Sb in Pb is 5.8 at. pct and Pb in Sb is 1.9 at. pct at eutectic temperature. They exhibit different temperature-dependent molar volumes and surface energies. Hence, some of these assumptions considered in the model are not valid for the present system. Therefore, for evaluating the size-dependent nanoscale phase diagram, modification of the above-mentioned theoretical approach was made.

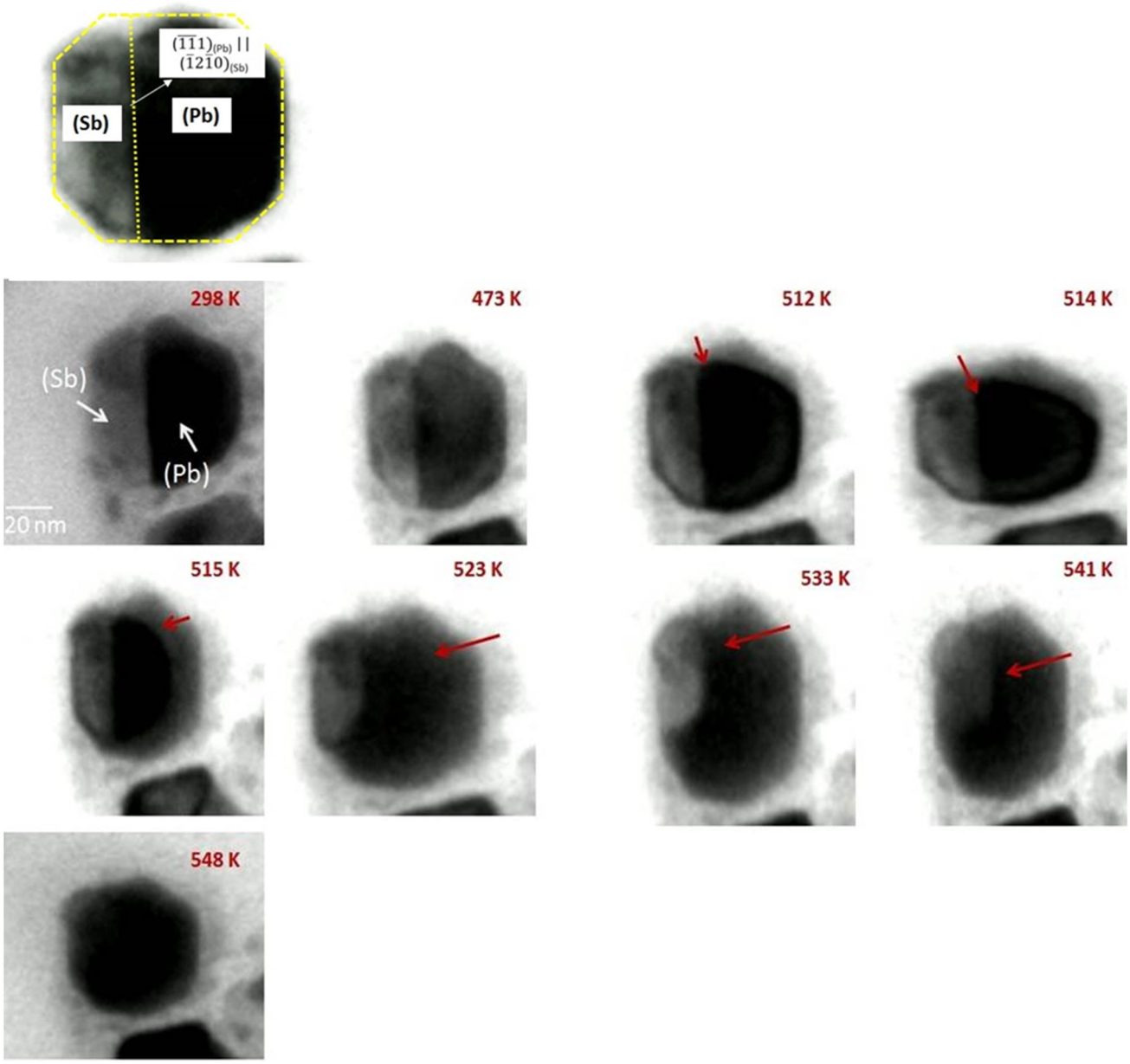

Fig. 5—A series of TEM micrographs showing melting within a Pb-Sb nanoparticle during the *in situ* heating experiment.

Weissmuller *et al.*[37] utilized the free energy per nanosize particle given below

$$\overleftarrow{G}(T,n,x) = nGm(T,x) + \sum_j \sigma_j(x,T)A_j(T,n,x) \qquad [1]$$

where $\overleftarrow{G}(T,n,x)$ represents the Gibbs free energy per particle in single-phase state (solid or liquid) at temperature T with a fixed amount of matter ($n = n^{\alpha} + n^{\beta}$) per particle, G^m denotes the molar free energy, A_j is the interfacial area of the particle, and σ_j is interfacial energy. In the present case, each particle comprises two coexisting phases as shown in Figure 1. For the bulk system, the total Gibbs free energy (G^{total}) of two coexisting phases at arbitrary composition can be expressed as

$$G^{\text{total}}(T,n,x) = \frac{n^{\alpha}}{n}G^{\alpha} + \left(1 - \frac{n^{\alpha}}{n}\right)G^{\beta} \qquad [2]$$

To perform the calculation, let us use the symbols α and β for (Pb) and (Sb) phase, respectively. $\frac{n^{\alpha}}{n}$ represents the phase fraction of α, which can be calculated using the lever rule.

In the present case, the particles are nanosized, and each particle comprises two distinct phases. Therefore, the interfacial energy between them can no longer be neglected. The creation of additional interfaces within the particle can alter the equilibrium conditions. Thus, the total free energy is no longer a linear function of the phase fraction. For the nanoscale system, Eq. [2] is

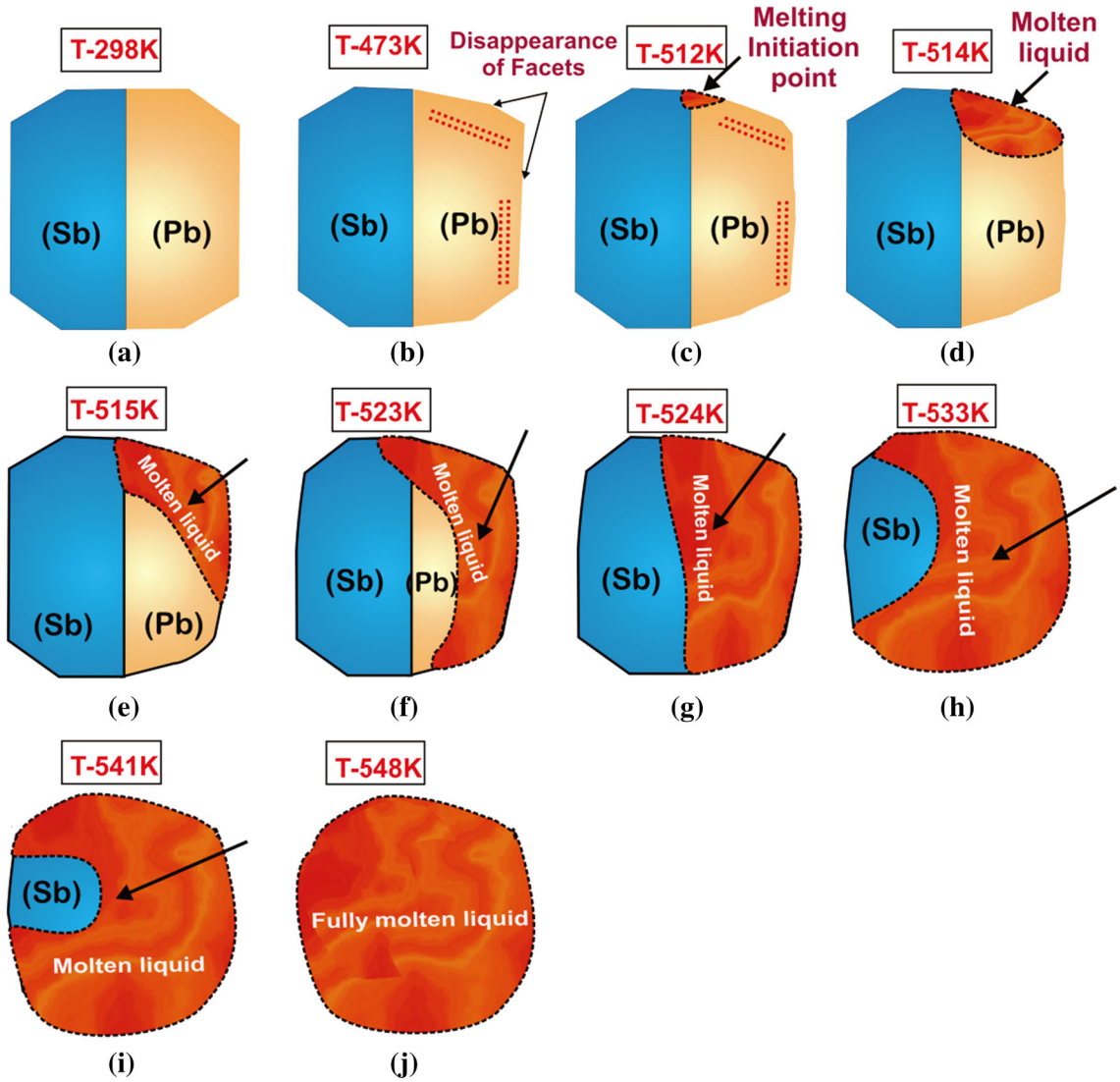

Fig. 6—(*a* to *j*) Schematic illustration of the melting process of multiphase Pb-Sb free alloy nanoparticles.

Table III. Thermodynamic and Physical Properties Used in the Calculation of Surface Energies of Pb-Sb Binary Alloy Systems

Variables	Function	References
Surface Energy (J/m^2)	$\sigma^{L}_{Pb} = 0.4975 - 1.096 * 10^{-4}T$	44
	$\sigma^{s}_{Pb} = 0.5396 - 1.096 * 10^{-4}(T - 600.46)$	calculated
	$\sigma^{L}_{sb} = 0.4190 - 0.561 * 10^{-4}T$	44
	$\sigma^{s}_{sb} = 0.460375 - 0.561 * 10^{-4}(T - 903.63)$	calculated
Molar Volume (m^3/mol)	$V^{L}_{Pb} = 19.42 * 10^{-6}\{1 + 0.000124(T - 600.46)\}$	45
	$V^{s}_{Pb} = 1.87072 * 10^{-5}\{1 + 0.000124(T - 600.46)\}$	calculated
	$V^{L}_{sb} = 1.88 * 10^{-5}\{1 + 0.00013(T - 903.8)\}$	45
	$V^{s}_{sb} = 1.81906 * 10^{-5}\{1 + 0.00013(T - 903.8)\}$	calculated

modified by adding the total surface free energy (σA) term. Thus, the total Gibbs free energy of a nanoparticle consisting of two phases can be calculated by:

$$G^{\text{total}}(T,n,x) = \frac{n^{\alpha}}{n}G^{\alpha} + \left(1 - \frac{n^{\alpha}}{n}\right)G^{\beta} + \sum_{j}\sigma_{j(x,T)}A_j(T,n,x) \qquad [3]$$

For biphasic alloy nanoparticles, four possible states exist and the four corresponding free energy functions are: $G^{\text{total},\alpha\beta}$, $G^{\text{total},\alpha l}$,$G^{\text{total},\beta l}$and $G^{\text{total},l}$where α, β and L represent the solid phases and liquid phase, respectively. These four free energies were calculated as a function of the phase fraction at each temperature. To determine

the free energies, the molar free energies (G^{m}) of mixing of FCC (*P*b) and rhombohedral (*S*b) were estimated by using the thermodynamic functions provided in Table IV.[38,39]

Furthermore, in Eq. [3], the second term can be expanded:

$$\sum_{j} \sigma_j(x,T)A_j(T,n,x) = A^{\alpha}\sigma^{\alpha} + A^{\beta}\sigma^{\beta} + A^{\alpha/\beta}\sigma^{\alpha/\beta} \quad [4]$$

Here, A^{α}andA^{β}represent the surface area of α and β phases, respectively, and $A^{\alpha/\beta}$ indicates the interface-interphase area, while σ^{α}, σ^{β} represents the corresponding specific surface energies of the α, β phases and $\sigma^{\alpha/\beta}$is the specific interfacial energy between α and β phases. Each function of Eq. [4] was evaluated by adopting the following approximation: (1) the surface and interface area can be estimated by using the *in situ* TEM images (as shown in Figure 5) of Pb-Sb binary alloy nanoparticles. Surface areas are predicted as a function of temperature (T) assuming a constant eutectic composition (x_e) of the system. It is clearly evident from the TEM images that the morphology of the nanoparticle is cap-on-body geometry. The surface area can be deduced by knowing the actual shape of the nanoparticle. Here, the majority of particles shapes were cuboctahedral (in Figure 5). The absolute surface area (A) of a cuboctahedral shape with an edge length of l is given by $A = [6+2/\sqrt{3}]\, l^2$. The diameter of the enclosed sphere can be employed as a measure of nanoparticle size. The diameter is given by $D_s = 1.12l$.[40] In the calculation, the particle shape is considered to be a cuboctahedron. The *in situ* TEM images clearly reveal that as the temperature increases, the particle shape starts to change. At high temperature, the shape changes from a cuboctahedron to being nearly spherical. However, the difference in the surface area between the spherical and cuboctahedron shape is approximately 5.7 pct. It was also found that the surface areas of the nanoparticle in different shapes were different even at the identical volume.[41] (2) The interface area ($A^{\alpha/\beta}$) can be assumed to be flat and defined by the length measurement from the TEM images. (3) σ^{α}, σ^{β} and $\sigma^{\alpha/\beta}$ also strongly depend on the composition of the phases. The change of surface and interfacial energies due to compositional change will be significant and needs to be considered. For eutectic Pb-Sb, $\sigma^{\alpha/\beta}$ has been reported to be 0.141 J/m^2 at room temperature in the literature.[42] For calculation, this value was presumed to be constant for all temperatures. Furthermore, to evaluate the nanophase diagram, an estimation of surface energies(σ^{α}, σ^{β}) as a function of the composition of both phases is required. When the nanoparticles comprise the interface among the phases, the mole fraction and composition of the leading phases depend on the average composition of the nanoparticles. The composition and mole fraction together determine the total surface energies.[30] Since the surface makes an important contribution to the total Gibbs free energy of the particles, nanoparticles with different average compositions will lead to distinct surface energies and consequently different solubility ranges compared with the bulk system. Therefore, the surface energies of α, β for the 17.5 at. pct Pb-Sb alloy, σ^{α} and σ^{β}, were calculated using modified Butler's equations for binary alloys.[43] This equation expresses the surface energy in terms of equilibrium between the chemical potentials of the bulk components and their surface at different compositions. Butler's equation is given below:

$$\sigma = \sigma_{Pb} + \frac{RT}{A_{Pb}}\log e\left(\frac{1-x_{sb}^{s}}{1-x_{sb}^{b}}\right) + \frac{1}{A_{Pb}}\left[\Delta G_{Pb}^{s}\left(T,x_{Pb}^{s}\right) - \Delta G_{Pb}^{b}\left(T,x_{Pb}^{b}\right)\right] \quad [5a]$$

$$\sigma = \sigma_{sb} + \frac{RT}{A_{sb}}\log e\left(\frac{1-x_{Pb}^{s}}{1-x_{Pb}^{b}}\right) + \frac{1}{A_{sb}}\left[\Delta G_{sb}^{s}\left(T,x_{sb}^{s}\right) - \Delta G_{sb}^{b}\left(T,x_{sb}^{b}\right)\right]. \quad [5b]$$

where$R$ is the universal gas constant (8.31 Jmol^{-1}K^{-1}), and T is the temperature. σ_{Pb} and σ_{Pb} are the interfacial energies, and A_{Pb} and A_{sb} are the molar surface areas of pure Pb and Sb, respectively. x_{Pb}^{b} and x_{Pb}^{s} are the mole fractions of component Pb at bulk and the surface, respectively. $\Delta G_{Pb}^{b}\left(T,x_{Pb}^{b}\right)$ and $\Delta G_{Pb}^{s}\left(T,x_{Pb}^{s}\right)$ are the partial excess Gibbs free energy of Pb for the bulk and surface, respectively. Similarly, the parameter for Sb can also be defined. Using the above-described Eq. [5a], the temperature- and composition-dependent surface energies (σ^{α} and σ^{β}) can be calculated. The physical properties used in the calculation are summarized in Table III.[44,45] Details of the calculation are discussed in the Appendix. Employing all the relevant and estimated data in Eqs. [5a] and [5b], the composition-dependent surface energies of Pb-Sb are estimated for temperatures ranging from 300 K to 1000 K. Figure 7(a) shows the plot of the surface energy of Pb-rich solid solution (Pb) with respect to the mole fraction of Sb at different temperatures whereas that of the Sb-rich solid solution is presented in Figure 7(b). One can clearly see that there is a small deviation at temperatures around 300 K and 400 K due to the limited solubility in the conventional Pb-Sb phase diagram at low temperature. The surface energy of the alloy deviated positively for α-phase and negatively for β-phase from the value predicted by the concentrated weight average at all the temperatures investigated.

Let us now focus our attention on the calculation of the size-dependent nanoalloy phase diagram. With the knowledge of interface and surface energies, free energies of all the possible states ($G^{\text{total},\alpha\beta}$, $G^{\text{total},\alpha l}$,$G^{\text{total},\beta l}$ and $G^{\text{total},l}$) of the alloy were evaluated and computed. The absolute minimum of the Gibbs free energy at a given value of temperature and composition for different particle sizes (r = radius) is obtained from the tangent to curve construction rule. The calculations carried out for r = 80, 60, 45 and 30 nm are shown. The results are shown in Figure 8, in which the phase diagrams of the bulk Pb-Sb system and nanoparticles

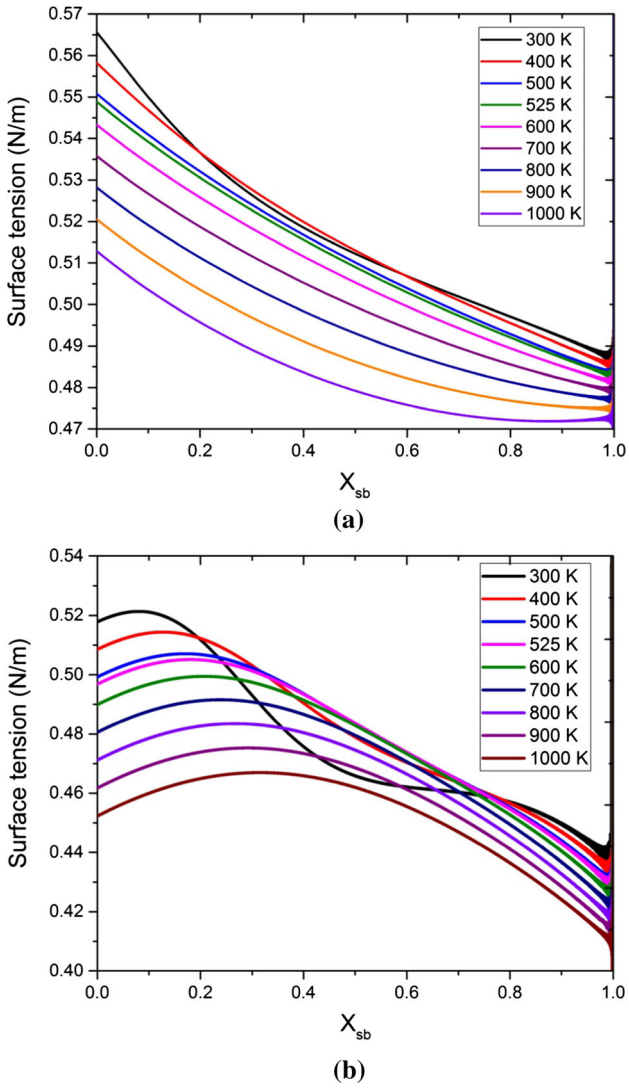

Fig. 7—(*a*) Calculated interface energy of Pb-rich solid solution phase (Pb) and (*b*) calculated interface energy of Sb-rich solid solution phase (Sb) at different temperatures.

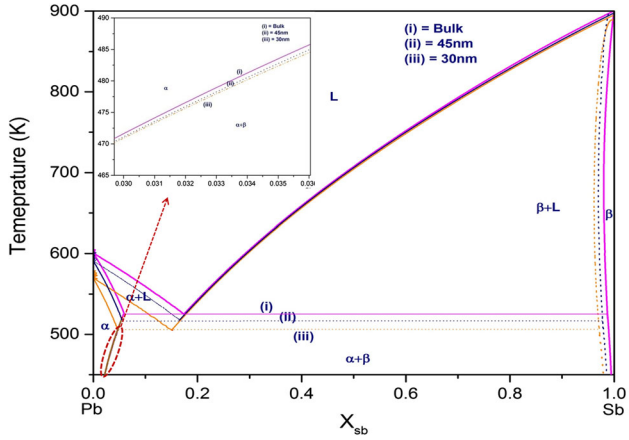

Fig. 8—Calculated nanophase diagram of the Pb-Sb alloy system.

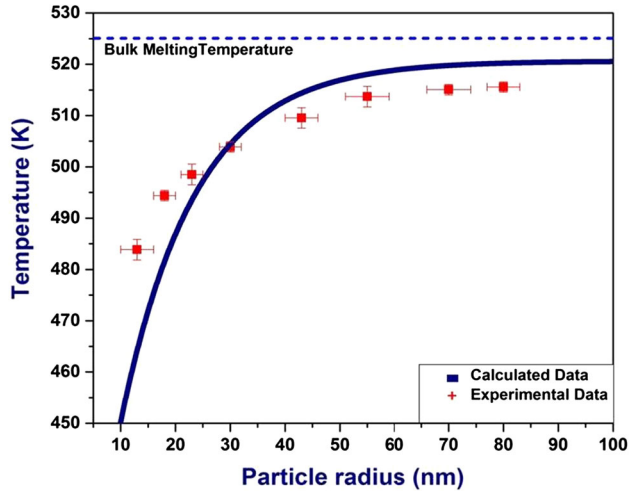

Fig. 9—Melting temperature of Pb-Sb alloy as a function of particle size.

having a particle radius of 45 and 30 nm nanoparticle size are shown. Figure 8 demonstrates that the shift of temperature and composition occur as the particle size reduces from bulk to 30 nm.

As mentioned previously, several attempts were made to understand the size-dependent melting temperature of the nanoparticle.[23,24,26] Similarly, an effort was made in the present investigation to determine a quantitative relationship between the melting temperature of the alloy nanoparticle and particle size. Figure 9 shows the comparison between the experimentally obtained results and theoretical calculated results for the size-dependent melting temperature as a function of nanoparticle size (r). The experimental data (red bulleted points) were obtained from DSC analyses of all the samples. The eutectic temperature of the bulk alloy (blue dotted line) is also shown in Figure 9.

In this plot, the experimental results bear closer resemblances to the theoretically calculated ones predicted using a nanophase diagram. However, a small discrepancy between the experimental and theoretical result was observed. This may be because the following assumptions were not met during the theoretical calculation. The curved interfaces of the phases were not considered. The surface and interfacial segregation was considered insignificant with respect to the volume of the system. The relative stability of the phase configuration with respect to the other (*i.e.*, core shell configuration vis-à-vis the cap-on-body configuration) was not compared. In addition, the complexities of the real system (interaction of neighboring nanoparticles, which is not considered in these models) were not considered. Even non-availability of all the necessary parameters such as the exact interfacial energy can lead to deviation. The interfacial energy between α and β phase and $\sigma^{\alpha/\beta}$ of the eutectic system also plays a role in the lowering of the melting temperature as a function of size. In general,

the interface energies are larger in magnitude than the surface energies because of the capillary effect present at the interface between the coexisting phases, which further leads to a larger contribution of the surface to the total Gibbs free energy.[30] Recently, it has also been reported that the size-dependent melting temperature of eutectic alloy nanoparticles decreases more rapidly with decreasing particle size compared with the constituent pure system or single-phase nanoparticles of similar size.[46,47] As the particle size decreases from bulk to the nanoscale, the relative contribution of the interfacial energy between two phases reaches a higher value because of their extremely large surface area-to-volume ratio. As a consequence, the Gibbs free energy of the single-phase alloy nanoparticle will be lower than the Gibbs free energy of the two-phase alloy nanoparticles. Thus, the accurate determination of the interfacial energy between α and β phase is also one of the most important parameters for the prediction of the melting temperature.

V. CONCLUSIONS

In the present investigation, we have synthesized Pb-17.5 at. pct Sb multiphase free alloy nanoparticles by the solvothermal route. Furthermore, the as-synthesized sample was heat-treated at 373 K for different times to obtain different ranges of particle size. Size-dependent melting behavior of the alloy nanoparticle has been systematically studied by combining the experimental and theoretical models. The significant observations obtained in the present study can be summarized as follows:

i. DSC has been extensively utilized to determine the melting temperature of the Pb-17.5 at. pct Sb alloy nanoparticles. The melting temperature has been observed to be size dependent. Smaller alloy nanoparticles exhibit more depression in melting temperature than larger nanoparticles.
ii. *In situ* TEM heating clearly reveals depression of the melting temperature of the bi-phasic nanoparticles. The melting was initiated at the outer surfaces of the biphasic particles and spread first along (Pb) having relatively lower melting temperature. The (Sb) phase subsequently melts.
iii. A size-dependent phase diagram was obtained using theoretical modeling. Subsequently, experimentally observed size-dependent melting behavior of alloy nanoparticles was compared with the theoretical calculation. A reasonably close match between the theory and experimental result was observed.

ACKNOWLEDGMENTS

Authors would like to thank Prof. K. Chattopadhyay and Dr. S. Kashyap for helping in the *in situ* TEM measurement. Authors would like to thank Advance Imaging Centre at IIT Kanpur and office of Dean R&D for microscopic facilities.

DATA AVAILABILITY

The raw/processed data required to reproduce these findings cannot be shared at this time because of technical limitations during submission. The raw and processed data required to reproduce these findings will be made available to download from http://home.iitk.ac.in/~kbiswas/.

APPENDIX

Details of Thermodynamics Calculations

The objective of the appendix is to describe the details and procedure for obtaining the nanophase diagram using a thermodynamic database of molar volume and surface tensions of the respective pure metals. The method is adapted from the model developed by Weissmuller *et al.*[37]

The molar free energy, G^{m}, of a regular solution is commonly derived as:

$$\begin{aligned} G^{\mathrm{m}}(x,T) = {} & x^{\circ}_{\mathrm{Pb}} G_{\mathrm{Pb}} + (1-x_{\mathrm{Pb}})^{\circ}G_{\mathrm{sb}} \\ & + RT(x_{\mathrm{Pb}}\ln x_{\mathrm{Pb}} + (1-x_{\mathrm{Pb}})\ln(1-x_{\mathrm{Pb}})) \\ & + G^{xs}_{mix} \end{aligned} \qquad [A1]$$

where x indicates the mole fractions of components and $^{\circ}G_{\mathrm{Pb}}$ and $^{\circ}G_{\mathrm{sb}}$ are the standard Gibbs free energies of the pure components Pb and Sb, respectively. T is the temperature, R is the universal gas constant, and G^{xs}_{mix} is the excess Gibbs free energy of mixing, which is extended by the Redlich-Kister formalism[48] as:

$$G^{xs}_{mix} = x_{\mathrm{Pb}}(1-x_{\mathrm{Pb}}) \sum_{\vartheta} \Omega_{\vartheta}(2x-1)^{\vartheta} \qquad [A2]$$

where Ω_{ϑ} is a non-ideal interaction parameter. ϑ is the order of expansion where for regular solution phases $\vartheta = 0$ and $\vartheta = 1$ for non-regular solution phases. Thermodynamic functions used during calculation are tabulated in Table IV.

To evaluate the surface energies of solid phases (σ^{α} and σ^{β}) by using Butler's equation, the molar surface area, surface energy and partial excess free energy of the pure component Pb or Sb need to be determined first. Therefore, the molar surface area can be calculated by using the following equation, $A_i = 1.091 N_{\mathrm{A}}^{\frac{1}{3}} (V_i)^{\frac{2}{3}}$, where N_{A} and V_i are Avogadro's number and the molar volume of component i. The molar volume$V$ is estimated by:

$$V = x_{\mathrm{Pb}} V_{\mathrm{Pb}} + (1-x_{\mathrm{Pb}}) V_{\mathrm{sb}} \qquad [A3]$$

V_{Pb} and $V_{\mathrm{sb}}$are the molar volumes of the pure components of Pb and Sb. The values of the molar volume of pure Pb and Sb in liquid state from the reported literature were used.[45,49] For evaluating the molar volume of pure components Pb and Sb in solid state, the following equation was used:

Table IV. Thermodynamic Functions Used in the Calculation of the Nano-Phase Diagram are Summarized in the Table

Standard Element Reference Gibbs Free Energies[38]	
FCC	
$G^{o}_{pb\ (Solid)}$ =	− 7650.085 + 101.700244 T − 24.5242231 T ln(T) − 3.65895E-3 T^2 − 0.24395E-6 T^3 (298.15 < T < 600.61)
	− 10531.095 + 154.243182 T − 32.4913959 T ln(T) + 1.54613E-3 T^2 + 805.448E23 T^{-9} (600.61 < T < 1200)
$G^{o}_{pb\ (Liquid)}$ =	− 2977.961 + 93.949561 T − 24.5242231 T ln(T) − 3.65895E-3 T^2 − 0.24395E-6 T^3 − 60.19E-20 T^7 (298.15 < T < 600.61)
	− 5677.958 + 146.176046 T − 32.4913959 T ln(T) + 1.54613E-3 T^2 (600.61 < T < 1200)
$G^{o}_{sb\ (Solid)}$ =	10631.142 + 142.454689 T − 30.5130752 T ln(T) + 7.748768E-3 T^2 − 3.003415E-6 T^3 + 100625 T^{-1} (298.15 < T < 903.78)
Rhombohedral	
$G^{o}_{pb\ (Solid)}$ =	− 7350.085 + 102.700244 T − 24.5242231 T ln(T) − 3.65895E-3 T^2 − 0.24395E-6 T^3 (298.15 < T < 600.61)
	− 10231.095 + 155.243182 T − 32.4913959 T ln(T) + 1.54613E-3 T^2 + 805.448E23T^{-9}(600.61 < T < 1200)
$G^{o}_{sb\ (Solid)}$ =	− 9242.858 + 156.154689 T − 30.5130752 T ln(T) + 7.748768E-3 T^2 − 3.003415E-6 T^3 + 100625 T^{-1} (298.15 < T < 903.78)
$G^{o}_{sb\ (Liquid)}$ =	10579.47 + 134.231525 T - 30.5130752 T ln(T) + 7.748768E-3 T^2 − 3.003415E-6 T^3 + 100625 T^{-1} − 174.847E-22 T^7(298.15 < T < 903.78)
Interaction Parameters[39]	
Liquid	${}^{o}\Omega_{Pb,Sb}$ = −256.510 − 1.135690T
	${}^{1}\Omega_{Pb,Sb}$ = −150.577 + 0.017182T
	${}^{2}\Omega_{Pb,Sb}$ = 226.284 − 0.378119T
FCC A1(Pb)	${}^{o}\Omega_{Pb,Sb}$ = 6287.361 − 12.670708T
Rhombohedral A7 (Sb)	${}^{o}\Omega_{Pb,Sb}$ = 20733.193 − 4.376804T

$$V_x^{\mathrm{s}} = \frac{V_x^{\mathrm{L}}}{(1-\alpha_x)}\,(x = \mathrm{Pb, Sb}) \qquad [A4]$$

where α_x is the thermal expansion coefficient, which is a ratio of the change in volume of solid while melting, $\alpha_x = \frac{V^{\mathrm{L}}_{\mathrm{x,m.p}} - V^{\mathrm{s}}_{\mathrm{x,m.p}}}{V^{\mathrm{s}}_{\mathrm{x,m.p}}}$, where, $V^{\mathrm{s}}_{\mathrm{x,m.p}}$ and $V^{\mathrm{L}}_{\mathrm{x,m.p}}$ are the molar volumes of pure liquid and solid x (Pb or Sb) at melting temperature.

Furthermore, the surface energy values of pure Pb and Sb in liquid state were obtained directly from the literature.[44] Some of the reported references showed the surface energy value of the pure solid at the melting point is observed to be 25 pct larger than surface energy of the pure liquid.[49,50] Therefore, Eq. (A5) was used to approximate the surface energy of the pure solid component:

$$\sigma_x^{\mathrm{s}} = 1.25\sigma^{\mathrm{L}}_{x,m.p} + \frac{\partial \sigma_x^{\mathrm{L}}}{\partial T}\left(\mathrm{T} - \mathrm{T_{x,m.p}}\right) \quad x = \mathrm{Pb\ or\ Sb} \qquad [A5]$$

where $\sigma^{\mathrm{L}}_{x,m.p}$ is the surface energy of pure liquid x (Pb or Sb) at its equilibrium melting point $T_{x,m.p.}$.

All the reported and calculated temperature-dependent surface energies and molar volumes of the pure components (Pb, Sb) in the solid as well as liquid state are summarized in Table III.

The partial excess Gibbs free energy of components Pb and Sb in the bulk can be evaluated by Reference 49:

$$\Delta G^{\mathrm{b}}_{\mathrm{Pb}} = G^{xs}_{mix} - (1 - x_{\mathrm{Pb}})\frac{\mathrm{d}\left(G^{xs}_{mix}\right)}{\mathrm{d}x_B} \qquad [A6a]$$

$$\Delta G^{\mathrm{b}}_{\mathrm{sb}} = G^{xs}_{mix} + x_{\mathrm{Pb}}\frac{\mathrm{d}\left(G^{xs}_{mix}\right)}{\mathrm{d}x_A} \qquad [A6b]$$

For obtaining the partial excess Gibbs free energy of components Pb and Sb in the surface, Speiser, Yeum's model has been used. According to Yeum's model.[51,52]

$$\Delta G^{\mathrm{s}}_{\mathrm{Pb}} = \Omega^{mix}\Delta G^{\mathrm{b}}_{\mathrm{Pb}} \qquad [A7a]$$

$$\Delta G^{\mathrm{s}}_{\mathrm{sb}} = \Omega^{mix}\Delta G^{\mathrm{b}}_{\mathrm{sb}} \qquad [A7b]$$

$\Omega^{mix} = 0.85$; liquid alloy and $\Omega^{mix} = 0.84$; solid alloy

Ω^{mix} represents the ratio of the coordination number in the surface to that in the bulk.[49]

The surface energies of solid phases (σ^{α} and σ^{β}) can be calculated by setting all the values in Butler's Eqs. [A6a] and [A6b] computed by solving Eqs. [A3] through [A7a]. The equations are simultaneous equations with two unknowns: $x^{Surface}_{Pb,Sb}$ and$\gamma_{\alpha,\beta}$. Furthermore, these equations can be solved for those unknowns numerically.

The four possible states and corresponding free energy functions are given by$G^{\mathrm{total},\alpha\beta}$, $G^{\mathrm{total},\alpha l}$, $G^{\mathrm{total},\beta l}$ and $G^{\mathrm{total},l}$. These four free energies were calculated as a function of the phase fraction at each temperature. Let us assume p_1 and p_2, the terminal mole fraction of the Pb- and Sb-rich phases, respectively. Here, p_1 and p_2 correspond to the intercepts of a common tangent with the free energy curve. To approximate the two minima of the Gibbs free energy curves, the following coupled equations are utilized:

$$\left.\frac{dG^{\mathrm{total}}(x)}{dx}\right|_{\mathrm{x}=p_1} = \left.\frac{dG^{\mathrm{total}}(x)}{dx}\right|_{\mathrm{x}=p_2} \qquad [A8a]$$

$$\left.\frac{dG^{\mathrm{total}}(x)}{dx}\right|_{\mathrm{x}=p_1} * (p_1 - p_2) = G^{\mathrm{total}}(p_1) - G^{\mathrm{total}}(p_2) \qquad [A8b]$$

p_1 and p_2 are solved for ranges of temperature and plotted on a phase diagram as shown in Figure 8.

ELECTRONIC SUPPLEMENTARY MATERIAL

The online version of this article (https://doi.org/10.1007/s11661-019-05275-0) contains supplementary material, which is available to authorized users.

REFERENCES

1. F. Calvo: *Phys. Chem. Chem. Phys.*, 2015, vol. 17, pp. 27922–39.
2. O.V. Salata: *J. Nanobiotechnol.*, 2004, vol. 2, pp. 1–6.
3. A. Akbarzadeh, M. Samiei, and S. Davaran: *Nanoscale Res. Lett.*, 2012, vol. 7, p. 144.
4. A. Patel, P. Prajapati, and R. Boghra: *Asian J. Pharm. Clin. Res.*, 2011, vol. 1, pp. 40–55.
5. S.R. Sahu, M.M. Devi, P. Mujkherjee, P. Sen, and K. Biswas: *J. Nanomater.*, 2013, vol. 6, pp. 1–9.
6. K. Biswas, G. Phanikumar, K. Chattopadhyay, T. Volkmann, O. Funke, D. Holland-Moritz, and D.M. Herlach: *Mater. Sci. Eng. A*, 2004, vol. 375, pp. 464–67.
7. K. Biswas, G. Phanikumar, D. Holland-Moritz, and D.M. Herlach Chattopadhyay: *Philos. Mag.*, 2007, vol. 87, pp. 3817–37.
8. P. Sharma, K. Biswas, A.K. Mondal, and K. Chattopadhyay: *Scripta. Mater.*, 2009, vol. 166, pp. 600–03.
9. M.M. Devi and K. Biswas: *Mater. Res.*, 2015, vol. 18, pp. 55–60.
10. W. Jesser, R. Shneck, and W. Gile: *Phys. Rev. B.*, 2004, vol. 69, p. 144121.
11. J. Sopousek, J. Vrestal, A. Zemanova, and J. Bursi: *J. Min. Metall. B.*, 2012, vol. 48, pp. 419–25.
12. V. Bhattacharya and K. Chattopadhyay: *Mater. Sci. Eng. A*, 2007, vol. 449, pp. 1003–08.
13. V. Bhattacharya and K. Chattopadhyay: *J. Nanosci. Nanotechnol.*, 2007, vol. 7, pp. 1736–43.
14. P.Y. Khan, V. Bhattacharya, K. Biswas, and K. Chattopadhyay: *J. Nanoparticle Res.*, 2013, vol. 15, pp. 1–15.
15. P.Y. Khan and K. Biswas: *Philos. Mag.*, 2014, vol. 94, pp. 2031–45.
16. P.Y. Khan: K. Biswas*J. Nanosci. Nanotechnol.*, 2015, vol. 15, pp. 309–16.
17. K. Chattopadhyay, V. Bhattacharya: *Encyclopedia Nanosci. Nanotechnol.*, 2004, pp. 217–32.
18. G. Allen and W. Jesser: *J. Cryst. Growth*, 1984, vol. 70, pp. 546–51.
19. S. Ali, V. Myasnichenko, and E. Neyts: *Phys. Chem. Chem. Phys.*, 2016, vol. 18, pp. 792–800.
20. T.E. Song, G. Wilde, and M. Peterlechner: *Appl. Phys. Lett.*, 2014, vol. 105, pp. 1–5.
21. N. Oehl, P. Michalowski, M. Knipper, J. Kolny-Olesiak, T. Plaggenborg, and J.R. Parisi: *J. Phys. Chem. C*, 2014, vol. 118, pp. 30238–43.

22. S. Bajaj, M.G. Haverty, R. Arróyave, and S. Shankar: *Nanoscale*, 2015, vol. 7, pp. 9868–77.
23. B. Kim, J. Tersoff, C.-Y. Wen, M. Reuter, E. Stach, and F. Ross: *Phys. Rev. Lett*., 2009, vol. 103, pp. 1–4.
24. J. Park and J. Lee: *Calphad*, 2008, vol. 32, pp. 135–41.
25. A. Shirinyan and M. Wautelet: *Mater. Sci. Eng. C*, 2006, vol. 26, pp. 735–38.
26. Y. Dahan, G. Makov, and R. Shneck: *Calphad*, 2016, vol. 53, pp. 136–45.
27. N. Braidy, G.R. Purdy, and G.A. Botton: *Acta Mater*., 2008, vol. 56, pp. 5972–83.
28. T. Massalski: *Binary Alloy Phase Diagrams*, 3rd ed., Metals Park, ASM International, 1992, pp. 206–10.
29. MM Devi and K Biswas: *Mater. Chem. Phys*., 2015, vol. 166, pp. 207–14.
30. G Wilde, P Brunzel, H Rössner, and J Weissmüller: in *Phase Transformations in Multicomponent Melts*, DM Herlach, ed., Wiley, Weinheim, 2008, pp. 87–106.
31. D.A. Porter, K.E. Easterling, and M. Sherif: *Phase Transformations in Metals and Alloys*, 3rd ed., CRC Press, New York, 2009, pp. 31–41.
32. V. Bhattacharya, E. Yamasue, K. Ishihara, and K. Chattopadhyay: *Acta Mater*., 2005, vol. 53, pp. 4593–4603.
33. J. Lee and H. Mori: *Vac. Sci. Technol. A*, 2003, vol. 21, pp. 32–36.
34. V Bhattacharya and K Chattopadhyay: *Mater. Sci. Eng. A*, 2004, vol. 375, pp. 932–35.
35. J.G. Lee, H. Mori: *Eur. Phys. D Atomic Mol. Opt. Plasma Phys*., 2005, vol. 34, pp. 227-30.
36. P. Bhattacharya, V. Bhattacharya, and K. Chattopadhyay: *J. Mater. Res*., 2002, vol. 17, pp. 2875–83.
37. J. Weissmüller, P. Bunzel, and G. Wilde: *Scr. Mater*., 2004, vol. 51, pp. 813–18.
38. A.T. Dinsdale: *Calphad*, 1991, vol. 15, pp. 317–425.
39. S. Hassam, D. Boa, Y. Fouque, K. Kotchi, and J. Rogez: *J. Alloy. Comput*., 2009, vol. 476, pp. 74–78.
40. H.M. Cundy and A.P. Rollett: *Mathematical Models*, Clarendon Press, Oxford, 1961, p. 161.
41. W. Qi and M. Wang: *Mater. Chem. Phys*., 2004, vol. 84, pp. 280–84.
42. L. Mondolfo, N. Parisi, and G. Kardys: *Mater. Sci. Eng*., 1985, vol. 68, pp. 249–66.
43. J. Butler: *Proc. R. Soc. Lond. Ser. A*, 1932, vol. 135, pp. 348–75.
44. R. Picha, J. Vřešťál, and A. Kroupa: *Calphad*, 2004, vol. 28, pp. 141–46.
45. M. Ghasemi, Z. Zanolli, M. Stankovski, and J. Johansson: *Nanoscale*, 2015, vol. 7, pp. 17387–96.
46. C. Chen, J.-G. Lee, K. Arakawa, and H. Mori: *Appl. Phys. Lett*., 2011, vol. 99, pp. 1–3.
47. C. Chen, J.-G. Lee, K. Arakawa, and H. Mori: *Appl. Phys. Lett*., 2011, vol. 98, p. 083108.
48. O. Redlich and A. Kister: *Ind. Eng. Chem. Res*., 1948, vol. 40, pp. 345–48.
49. T Tanaka: *Mater. Sci. Forum*, 2010, vol. 653, pp. 55–75.
50. V. Kumikov and K.B. Khokonov: *J. Appl. Phys*., 1983, vol. 54, pp. 1346–50.
51. R. Speiser, D. Poirier, and K. Yeum: *Scr. Mater*., 1987, vol. 21, pp. 687–92.
52. K. Yeum, R. Speiser, and D. Poirier: *Mater. Sci. Eng. B*, 1989, vol. 20, pp. 693–703.